Tidal conversion and turbulence at a model ridge: direct and large eddy simulations

Narsimha R. Rapaka, Bishakhdatta Gayen and Sutanu Sarkar†

Mechanical and Aerospace Engineering, University of California, San Diego, La Jolla, CA 92093, USA

Direct and large eddy simulations are performed to study the internal waves generated by the oscillation of a barotropic tide over a model ridge of triangular shape. The objective is to go beyond linear theory and assess the role of nonlinear interactions including turbulence in situations with low tidal excursion number. The criticality parameter, defined as the ratio of the topographic slope to the characteristic slope of the tidal rays, is varied from subcritical to supercritical values. The barotropic tidal forcing is also systematically increased. Numerical results of the energy conversion are compared with linear theory and, in laminar flow at low forcing, they agree well in subcritical and supercritical cases but not at critical slope angle. In critical and supercritical cases with higher forcing, there are convective overturns, turbulence and significant reduction (as much as 25 %) of the radiated wave flux with respect to laminar flow results. Analysis of the baroclinic energy budget and spatial modal analysis are performed to understand the reduction. The near-bottom velocity is intensified at critical angle slope leading to a radiated internal wave beam as well as an upslope bore of cold water with a thermal front. In the critical case, the entire slope has turbulence while, in the supercritical case, turbulence originates near the top of the topography where the slope angle transitions through the critical value. The phase dependence of turbulence within a tidal cycle is examined and found to differ substantially between the ridge slope and the ridge top where the beams from the two sides cross.

Key words: internal waves, stratified turbulence, turbulent flows

---

1. Introduction

Internal tides are internal gravity waves generated by the interaction of an oscillating barotropic flow with bottom topography in a stratified fluid. Some of the energy converted from the barotropic tide to the baroclinic flow is locally trapped and dissipated due to small-scale turbulence near the topography while the rest is radiated away from the topography. The tidal energy thus radiated is considered to have a significant contribution to the mixing of the stably stratified ocean (Polzin *et al.* 1997; Munk & Wunsch 1998; Ledwell *et al.* 2000; Wunsch & Ferrari 2004). Enhanced conversion to internal tides is found near sea-mounts (Kunze & Toole 1997; Lueck & Mudge 1997), submarine ridges (Rudnick *et al.* 2003; Klymak *et al.* 2006), submarine

† Email address for correspondence: ssarkar@ucsd.edu

canyons (Polzin *et al.* 1996; Carter & Gregg 2002), continental slope (Cacchione, Pratson & Ogston 2002; Moum *et al.* 2002; Nash *et al.* 2004, 2007) and deep rough topography (Polzin *et al.* 1997; St. Laurent, Toole & Schmitt 2001).

Inviscid linear estimates of the tidal energy radiated from various bottom topographies are well established in the literature. Linearization requires that the product $\epsilon Ex \ll 1$ (Balmforth, Ierley & Young 2002) where the criticality parameter, $\epsilon = \tan\beta/\tan\theta$, is the ratio of the topographic slope $\tan\beta$ to the slope of internal wave characteristic $\tan\theta = \sqrt{(\Omega^2 - f^2)/(N_\infty^2 - \Omega^2)}$, and the excursion number, $Ex = U_0/\Omega l$, characterizes the ratio of the fluid excursion during a tidal cycle to the topographic length. Applications of linear theory (Bell 1975*a*,*b*; Balmforth *et al.* 2002; St Laurent & Garrett 2002; Llewellyn Smith & Young 2002; Khatiwala 2003) invoked weak topography approximation (WTA) that requires a shallow slope topography with $\epsilon \ll 1$ and topographic height much less than the vertical wavelength of the internal tide. Linear theory shows that the radiated internal wave energy flux is proportional to $\pi/\rho_0 U^2 h^2 \sqrt{(N^2 - \Omega^2)}4$ and provides analytical estimates of the proportionality coefficient, M. Supercritical slopes that occur at sites of steep topography, e.g. at the Hawaiian ridge, are also of interest and a key result of the analytical studies of Llewellyn Smith & Young (2003) and St Laurent *et al.* (2003) is that the wave energy flux at steep topography can be substantially larger than at gentle slopes. Pétrélis, Llewellyn Smith & Young (2006) estimated the conversion rate for two different topographies: a triangular and a polynomial ridge and performed a parametric study of the effect of the topography height and width as well as water depth. For the triangular ridge to be examined in the present study, they showed that, for low-to-moderate values of the ratio of ridge height h to water depth H, the normalized wave flux, M, is a weak function of slope angle in the subcritical regime, increases abruptly at critical slope and then increases slowly in supercritical topography. Echeverri *et al.* (2009) performed laboratory measurements of wave conversion at a two-dimensional ridge with subcritical to supercritical slopes and showed that, at low excursion number, results from experiment, computation and theory agreed well for the low modes. Small differences in velocity profiles were attributed to differences in higher modes.

Numerical process studies to study wave radiation and local losses have provided insights into nonlinear effects on wave conversion and frequency spectra. These simulations are at geophysical scales but employ large values of molecular viscosity to stabilize the algorithm so that turbulence is not permitted. Legg & Huijts (2006) employed two-dimensional simulations with the MIT model to quantify the effect of varying velocity amplitude over Gaussian topography of various aspect ratios and heights. They found that the numerical results showed good agreement in many respects with linear theory predictions, e.g. the proportionality of wave flux to U_0^2 and h^2, the increase of wave flux from subcritical slopes to supercritical slopes, and the appearance of high harmonics when the barotropic velocity increases. Narrow topography (strongly supercritical slope angle) had larger values of viscous dissipation (in laminar flow state) owing to high vertical wavenumber modes. Legg & Klymak (2008) further examined internal wave dynamics in the case of strongly supercritical topography with $\epsilon = 4$, low excursion number and low Froude number. Overturns and large values of viscous dissipation (laminar flow) were found near the top and in the lee, i.e. behind the obstacle with respect to the flow at the ridge top. It was proposed that breaking lee waves and transient hydraulic jumps that occur when $\epsilon \geqslant 3$ cause these overturns. In a following study, Klymak, Legg & Pinkel (2010) parameterized tidal dissipation in supercritical topography from nonlinear breaking of lee waves and assessed its role in two-dimensional simulations.
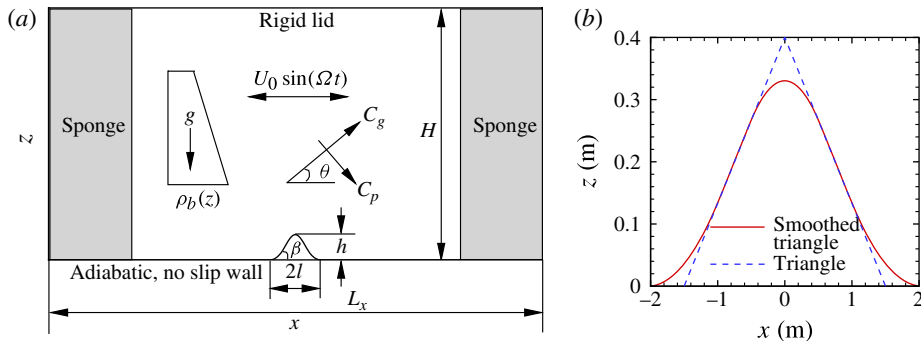
FIGURE 1. (Colour online) (*a*) Schematic of the problem: stratified fluid flows over a two-dimensional topography as a response to oscillatory forcing, $F_0(t_d)$, in the streamwise direction. (*b*) Profiles of the smoothed triangular topography (solid line) used in the present work and the triangular topography (dashed line) used by Pétrélis *et al.* (2006).

Three-dimensional, high-resolution simulations that resolve turbulence are necessary for numerical studies to help understand the microstructure associated with wave breaking. The first turbulence-resolving simulations of internal tide generation were performed by Gayen & Sarkar (2010) for flow over an asymmetric sloping bottom, corresponding to a model continental slope, at critical slope angle, i.e. $\epsilon = 1$. These simulations showed strong near-bottom intensification of the velocity and a strong outgoing internal wave beam similar to the laboratory experiment of Zhang, King & Swinney (2008). However, unlike the laboratory experiments, the simulations that were performed at higher Reynolds numbers showed transition to turbulence at $Re_s \equiv (U_0\sqrt{2\nu/\Omega})/\nu \simeq 100$. Both convective and shear instabilities were observed during different phases of the flow. Lim, Ivey & Jones (2010), using laboratory experiments, found beam formation, boundary-layer turbulence and upslope propagation of bores depending on the value of the Reynolds number. Gayen & Sarkar (2011*b*) employed direct numerical simulation (DNS)/large eddy simulation (LES) to demonstrate that the beam width, beam velocity and bottom turbulence energy and dissipation tend to increase with increasing length (height) of critical slope. Both Gayen & Sarkar (2010) and Gayen & Sarkar (2011*b*) employed a streamwise inhomogeneous formulation to model internal wave generation in contrast to the streamwise periodic domain employed by Slinn & Riley (1998) who performed the first turbulence resolving simulation of internal wave reflection. The mechanisms of turbulence generation at various phases during the oscillating flow over a sloping bottom are explained in the later work of Gayen & Sarkar (2011*a*) using LES of a small patch of an internal tidal beam, scaled up to a width of 60 m. Turbulent dissipation rate was found to peak when the near-bottom flow was near zero and reversed from downslope to upslope as in the observations of Aucan *et al.* (2006) at a bottom mooring on a deep flank at Kaena Ridge in Hawaii. Convective instability leading to overturns that span the internal wave beam was found to occur during flow reversal from down to up.

An outstanding question is how do nonlinear processes and bottom turbulence affect the internal wave generation and, in particular, what is the effect on the energy conversion to the baroclinic flow and on the wave flux radiated away from the topography? We address this question through turbulence-resolving simulations of oscillating flow over a smoothed triangular ridge, shown in figure 1(*b*). The symmetric triangular topography allows quantitative comparison with the linear theory results

of Pétrélis *et al.* (2006). Another important goal is to determine the phasing and energetics of the turbulence. The problem is formulated in §2, where the solution methodology is given and the simulated cases are listed. Methods, based on linear theory, to extract the mode strength and calculate the tidal conversion factor are briefly presented in appendix B. Results in the low-*Re* laminar flow regime are described and compared with linear theory for three values of criticality parameter in §3. In §4, changes in the conversion to internal waves at critical slope topography in higher-*Re* turbulent flow are discussed. Turbulence generation, phasing and energetics are discussed in §5. Supercritical slope topography in the turbulent regime is briefly addressed in §6. Finally, conclusions are presented in §7.

2. Formulation of the problem

The near-bottom flow resulting from a current oscillating over a two-dimensional ridge is illustrated in figure 1(*a*). The bottom is adiabatic while there is a background thermal stratification with constant buoyancy frequency, N_∞. The flow is forced by an imposed pressure gradient oscillating in time (t_d),

$$F_0(t_d) = \rho_0 U_0 \Omega \cos(\Omega t_d), \tag{2.1}$$

in the horizontal direction that results in a background barotropic current, $U(x)\sin(\phi)$, where ϕ is the tidal phase. Coordinates x, y and z denote the streamwise, spanwise and vertical directions and u, v and w are the corresponding velocity components. A larger view of the model ridge is shown in figure 1(*b*). The triangular ridge, without smoothing, can be described mathematically as

$$z(x) = \begin{cases} h_0 \left(1 - \dfrac{|x|}{l_0}\right) & \text{if } |x| \leqslant l_0, \\ 0 & \text{otherwise,} \end{cases} \tag{2.2}$$

where $h_0 = 0.4$ m and $l_0 = 1.5$ m. After smoothing, the ridge has a height of $h = 0.328$ m and a half-length of $l = 1.9$ m. The constant slope portion of the ridge ranges from $z = 0.13$ m to 0.28 m on both sides which correspond to $0.45 \leqslant |x| \leqslant 1.01$.

2.1. *Governing equations*

The dimensional quantities in the problem are the free stream velocity amplitude U_0, the tidal frequency Ω, the background density gradient $\mathrm{d}\rho_d^b/\mathrm{d}z_d|_\infty$ and the fluid properties molecular viscosity, ν, thermal diffusivity, κ, and density, ρ. The variables in the problem are non-dimensionalized as follows:

$$\left. \begin{array}{l} t = t_d \Omega, \quad \boldsymbol{x} = (x, y, z) = \dfrac{(x_d, y_d, z_d)}{U_0/\Omega}, \quad p^* = \dfrac{p_d^*}{\rho_o U_o^2}, \\[3mm] \boldsymbol{u} = (u, v, w) = \dfrac{(u_d, v_d, w_d)}{U_0}, \quad \rho^* = \dfrac{\rho_d^*}{\dfrac{U_0}{\Omega} \dfrac{\mathrm{d}\overline{\rho}_d}{\mathrm{d}z_d}\Big|_\infty}. \end{array} \right\} \tag{2.3}$$

The resulting non-dimensional form of the governing equations is as follows:

$$\nabla \cdot \boldsymbol{u} = 0 \tag{2.4a}$$

$$\frac{\mathrm{D}\boldsymbol{u}}{\mathrm{D}t} = -\nabla p^* + \cos(t)\boldsymbol{i} + \frac{1}{Re}\nabla^2 \boldsymbol{u} - B\rho^*\boldsymbol{k} - \nabla \cdot \boldsymbol{\tau} \tag{2.4b}$$

$$\frac{\mathrm{D}\rho^*}{\mathrm{D}t} = \frac{1}{Re\,Pr}\nabla^2 \rho^* + w - \nabla \cdot \boldsymbol{\lambda} \tag{2.4c}$$

Here, p^* denotes deviation from the background hydrostatic pressure and ρ^* denotes the deviation from the linear background state, $\rho^b(z)$.

The governing equations have three non-dimensional parameters: Reynolds number Re, Buoyancy parameter B and Prandtl number Pr, where

$$Re \equiv \frac{l_{ex}U_0}{\nu} = \frac{U_0^2}{\Omega\nu}, \quad B \equiv -g\frac{\mathrm{d}\rho_d^b}{\mathrm{d}z_d}\bigg|_\infty \frac{1}{\rho_0\Omega^2} = \frac{N_\infty^2}{\Omega^2}, \quad Pr \equiv \frac{\nu}{\kappa}. \tag{2.5}$$

Here, $l_{ex} = U_0/\Omega$ is the tidal excursion length and N_∞ is the background value of buoyancy frequency, assumed constant. The following Reynolds number,

$$Re_s = \frac{U\delta_s}{\nu} = \sqrt{2Re}, \tag{2.6}$$

based on the Stokes boundary layer thickness, $\delta_s = \sqrt{2\nu/\Omega}$, is a commonly used alternative to Re. The ridge geometry is given by the slope angle, β, and the slope length in the x-direction, l. The angle of the internal wave phase lines with the horizontal is given in a non-rotating environment by $\theta = \tan^{-1}\sqrt{\Omega^2/(N_\infty^2 - \Omega^2)}$. Thus, in addition to those listed in (2.5), there are three other independent non-dimensional parameters: the excursion parameter $Ex = U_0/(l\Omega)$, the slope angle β and the slope criticality parameter $\epsilon = \tan(\beta)/\tan(\theta)$. The topographic Froude number, $Fr = U_0/(N_\infty h)$, although not independent of the six non-dimensional parameters listed above, is also of interest.

The governing equation (2.4) are written in the following coordinates (see Gayen & Sarkar (2011b) for details) and transformed to the strong conservation law as described by Fletcher (1991):

$$\xi = \xi(x, z), \quad \eta = \eta(x, z), \quad \zeta = \zeta(y), \tag{2.7}$$

where, at the bottom topography, ξ points parallel to and across the ridge while η is normal to the ridge.

2.2. Numerical method

Transfinite interpolation (TFI) is used to generate the boundary conforming grid and the transformed governing equations are solved using a mixed spectral/finite difference algorithm as described by Gayen & Sarkar (2011b). Variable time stepping with a fixed Courant–Friedrichs–Lewy (CFL) number 0.8 is used. Time steps are the order of 10^{-3} s.

Periodicity is imposed in the spanwise ($\zeta = \zeta(y)$) direction on velocity, density ρ^* and pressure p^*.

The bottom boundary, $\eta = 0$, has zero velocity and zero density gradient. Grids are designed to be orthogonal near the boundary so that

$$\frac{\partial\rho}{\partial\eta} = 0 \Rightarrow \frac{\partial\rho^*}{\partial\eta} = -\frac{\partial\rho^b}{\partial\eta} \quad \text{at } \eta = 0. \tag{2.8}$$

At the top of the domain, $\partial u/\partial\eta = 0$, $v, w = 0$, and $\rho^* = 0$. At the left and right sides, $\partial u/\partial\xi = 0$, $v, w = 0$ and $\rho^* = 0$. To match the boundary condition for the density deviation, ρ^*, between the left and the bottom (similarly, the right and the bottom) boundaries, $\partial\rho^*/\partial\eta$ is set to zero at both the left and right ends of the bottom boundary, then it gradually reaches the value given by (2.8) within the width of the sponge layer from both of the ends and it is fixed at this value for the remaining extent of the bottom boundary. The pressure boundary conditions are $\partial p^*/\partial\eta = 0$ at the bottom and the top boundaries and $p^* = 0$ at the left and the right of the computational domain.

Rayleigh damping or a 'sponge' layer is used at the left and right boundaries of the computational domain as shown in figure 1(*a*) so as to minimize spurious reflections from the artificial boundary into the 'test' section of the computational domain. The velocity and scalar fields are relaxed towards the background state in the sponge region by adding damping functions $-\sigma(\xi, \eta)[u_i(\boldsymbol{x}, t) - 0]$ ($i = 2, 3$) and $-\sigma(\xi, \eta)[\rho^*(\boldsymbol{x}, t) - 0]$ to the right-hand side of the momentum and scalar equations, respectively. The value of $\sigma(\xi, \eta)$ is zero everywhere except in a region close to left and right boundary where it increases quadratically and reaches a maximum value corresponding to $\sigma(\xi, \eta)\Delta t \sim O(0.1)$ where Δt is the time step of the simulation. Since $\Delta t \sim O(10^{-3})$, it follows that $\sigma(\xi, \eta) \sim O(100)$.

The dynamic eddy viscosity model (Zang, Street & Koseff 1993; Vreman, geurts & Kuerten 1997) is used for the subgrid scale (SGS) stress tensor, $\boldsymbol{\tau}$, when the simulation is performed in LES mode. The SGS heat flux, $\boldsymbol{\lambda}$, is obtained using a dynamic eddy diffusivity model (Armenio & Sarkar 2002). The expressions for the SGS models are described by Gayen & Sarkar (2011*b*).

2.3. *Selection of simulated cases*

Table 1 gives important parameters of the simulations. Cases A–C are simulations performed at a fixed value of Re_s in the laminar flow regime, and the buoyancy frequency (N_∞) is varied to study the effect of the criticality parameter (ϵ). Cases A–C correspond to subcritical, critical and supercritical flow, respectively, with results to be compared with linear theory later. A different series of simulations, cases 1–7, are performed to assess the effect of increasing forcing amplitude U_0 and therefore Re_s. The criticality parameter shows that cases 1 to 7 are near-critical ($\epsilon \sim 1$) and have excursion number, $Ex \ll 1$, except for cases 6 and 7 where Ex is $O(0.1)$. In these cases, the buoyancy frequency is fixed and the barotropic free stream velocity U_0 is varied to study the effect of Re_s. Cases 4 and 5 are turbulent flow DNS while cases 6 and 7 correspond to a resolved-LES model with a dynamic eddy viscosity model. In order to assess the effect of forcing in the supercritical regime, cases 2sup, 4sup and 5sup are simulated with values of Re_s that match cases 2, 4 and 5, respectively.

The flow is statistically homogeneous in the spanwise direction and a y average is used to compute the time-dependent mean, $\langle \mathscr{A} \rangle_y(x, z, t)$, as follows:

$$\langle \mathscr{A} \rangle_y(x, z, t) = \frac{1}{L_y} \int_0^{L_y} \mathscr{A}(x, y, z, t) \, \mathrm{d}y. \qquad (2.9)$$

The turbulent fluctuations are inferred via departures of instantaneous velocity, pressure and density from the spanwise average. Statistics of turbulent quantities are a function of x and z, and are computed by spanwise averaging.

The computational domain lengths in the horizontal directions, L_x and L_y, and the vertical domain length, L_z which is equal to H, are specified in table 1. The spanwise domain length L_y is chosen so as to accommodate the largest possible spanwise vortical structures. Cases A–C and 1–3 are laminar flow simulations while cases 4–7 are turbulent flow simulations. The laminar flow simulations are over-resolved for consistency among grids; an order of magnitude lower spanwise resolution leads to less than 3 % change in the wave flux. The turbulent flow simulations require high resolution. Case 5 is a DNS with the distance to the first grid point from the wall $z_1^+ = 2.5$ in terms of the viscous wall unit ν/u_τ and minimum grid resolution in the streamwise direction $\Delta x_{min}^+ = 21$. Here, u_τ is the cycle average of the instantaneous friction velocity $(=\sqrt{\tau_w/\rho_0})$ based on the wall shear stress (τ_w) at the midslope.

Case	Re_s	U_0 (ms^{-1})	N_∞^2 (s^{-2})	ϵ	Ex	Fr	θ (deg)	N_x	N_y	N_z	Remark
A	30	0.021	5.6	0.57	0.011	0.0114	25	705	128	321	DNS
B	30	0.021	14.93	1.0	0.011	0.0043	15	705	128	321	DNS
C	30	0.021	67.33	2.17	0.011	0.0010	7	705	128	321	DNS
1	10	0.007	14.93	1.0	0.004	0.0014	15	705	128	321	DNS
2	30	0.021	14.93	1.0	0.011	0.0043	15	705	128	321	DNS
3	75	0.053	14.93	1.0	0.028	0.0108	15	705	128	321	DNS
4	100	0.071	14.93	1.0	0.037	0.0145	15	705	128	321	DNS, turbulent
5	177	0.125	14.93	1.0	0.066	0.0255	15	897	256	321	DNS, turbulent
6	300	0.212	14.93	1.0	0.112	0.0433	15	705	64	385	LES, turbulent
7	400	0.283	14.93	1.0	0.149	0.0578	15	705	64	385	LES, turbulent
2sup	30	0.021	67.33	2.17	0.011	0.0010	7	705	128	321	DNS
4sup	100	0.071	67.33	2.17	0.037	0.0032	7	705	128	321	DNS, turbulent
5sup	177	0.125	67.33	2.17	0.066	0.0057	7	705	128	385	DNS, turbulent

TABLE 1. Parameters of the simulated cases. In cases A–C, the criticality parameter is changed in the laminar flow regime by changing the stratification. In cases 1–7, the tidal forcing velocity, U_0, is progressively increased in the critical slope case. In cases 2sup–5sup, the tidal forcing is increased in the supercritical regime. For all cases: $L_x = 40$ m (30 m for cases 6 and 7), $L_y = 0.5$ m (0.25 m for cases 6 and 7), $L_z = H = 3.28$ m, $l = 1.9$ m, $h = 0.328$ m, $\beta = 15^o$, $\Omega = 1$ s^{-1}, $\nu = 10^{-6}$ m s^{-2} and $Pr = 1$. Note that the simulations are at the laboratory scale, for example, Ω and N_∞ are larger than those in the ocean but Ω/N_∞ takes values realized in the ocean. Similarly, the topographic length scales are small but the excursion number and Froude number correspond to deep oceanic wave generation sites of interest.
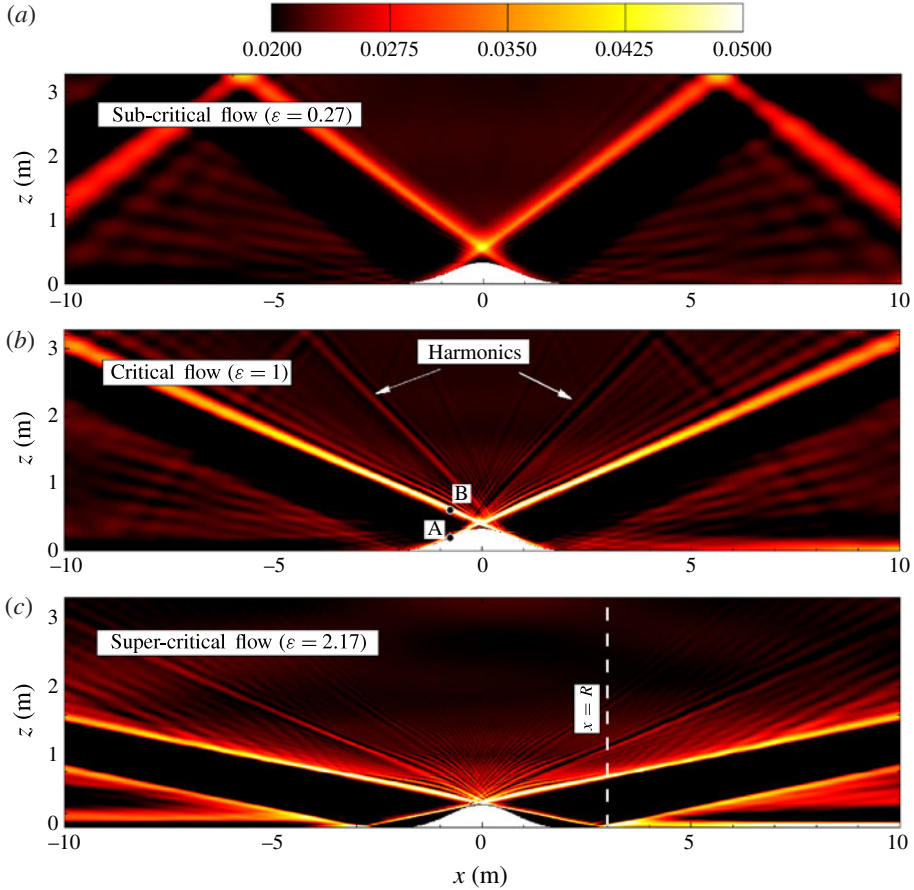
FIGURE 2. (Colour online) Streamwise velocity at $Re_s = 30$ in different flow regimes shown at time 51.75 s, phase of the barotropic velocity $\phi \approx \pi/2$. Frequency spectra at point A (midslope and in the boundary layer) and B (above point A and in the wave beam) will be shown later. Topography shown in white.

The spanwise direction has spectral accuracy with uniform grid spacing in physical space, $\Delta y^+ = 16$. Cases 6–7 correspond to a resolved-LES mode with a dynamic eddy-viscosity model.

3. Results in the laminar flow regime

3.1. *Effect of criticality on the internal wave structure at* $Re_s = 30$

The criticality parameter, ϵ, is an indicator of nonlinear response near the topography and determines the structure of the flow field such as formation of higher modes which combine to form an internal wave beam. For fixed geometry of the topography and forcing frequency, ϵ is varied by varying the level of stratification that determines the internal wave characteristic slope. At $Re_s = 30$, the flow remains laminar and two-dimensional. Figure 2(*a*–*c*) show the instantaneous streamwise velocity at $Re_s = 30$ in subcritical, critical and supercritical flow regimes, respectively. In subcritical flow, as shown in figure 2(*a*), internal waves originating near the topography radiate upward along the characteristic direction given by $\theta = \sin^{-1}(\Omega/N_\infty)$. The baroclinic response
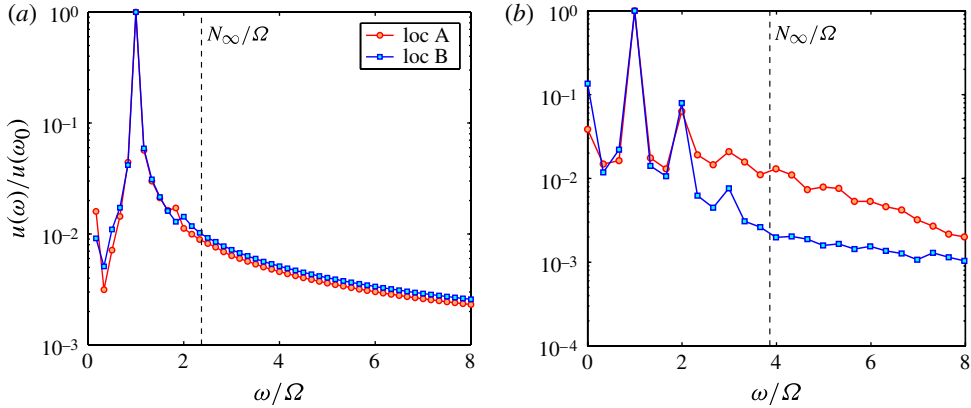
FIGURE 3. (Colour online) Frequency spectra for (*a*) subcritical flow and (*b*) critical flow at $Re_s = 30$. Point A is located in the boundary layer at midslope and point B is located vertically above A and in the beam as shown in figure 2(*b*).

in subcritical flow is weaker compared with the barotropic forcing. In critical flow, as shown in figure 2(*b*), since the internal wave characteristic slope matches with the topographic slope, resonant interaction of the internal wave with the topography generates higher spatial modes which combine to form an intensified internal wave beam. In supercritical flow, as shown in figure 2(*c*), resonant beam intensification occurs in a small region near the crest of the topography where the topographic slope is equal to the internal wave characteristic slope, and the beams are directed both upwards and downwards. The baroclinic response is significantly stronger in both critical and supercritical flow.

3.2. *Frequency spectra in laminar flow cases*

Fast Fourier transform (FFT) of the time series data of the streamwise velocity component is performed at two different points, A and B, shown in figure 2(*b*). The frequency spectra at locations A and B are shown in figure 3(*a*) for subcritical flow and in figure 3(*b*) for critical flow at $Re_s = 30$. In figure 3(*a*), at both locations A and B, the frequency spectrum has a sharp peak at the fundamental frequency. In figure 3(*b*), in addition to the peak at the fundamental frequency, the spectra has discrete peaks at higher harmonics that are below the buoyancy frequency ($N_\infty/\Omega = 3.9$). More than 99 % of the energy is contained at the fundamental frequency in cases with laminar flow. Hence, the modal decomposition (see appendix B) is performed solely for the velocity field corresponding to the fundamental frequency.

3.3. *Modal structure in laminar flow cases*

Figure 4(*a*) shows profiles of the baroclinic component of the vertical velocity field, computed using the procedure described in appendix A, at location $x = R = 3$ m, indicated in figure 2. In figure 4(*a*), the subcritical flow profile is dominated by modes 3–5 whereas critical and supercritical flow profiles suggest the superposition of several additional normal modes to represent the intensified beam. The positive narrow peak of $w(z)$ in critical flow at $z \approx 1.2$ m corresponds to the intensified beam at a fundamental frequency followed by a broad region of negative peak. The local peaks
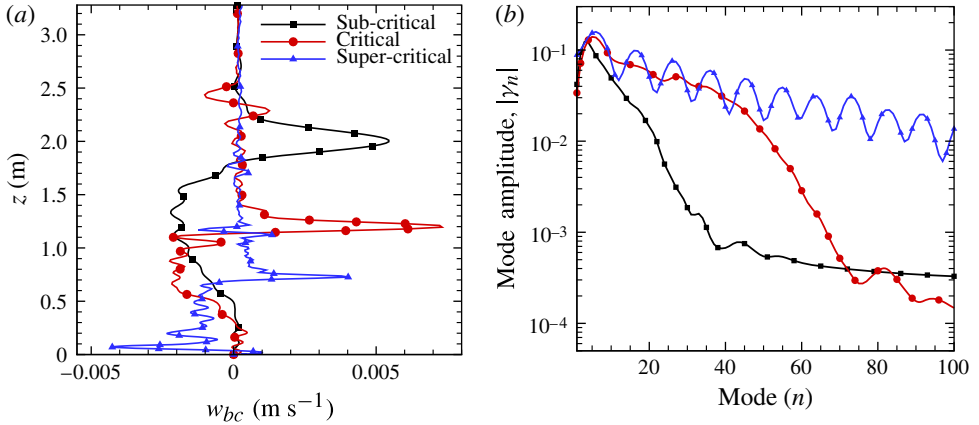
FIGURE 4. (Colour online) (*a*) Example profile of the baroclinic vertical velocity profile in the laminar case, $Re_s = 30$. Profile shown at $x = 3$ m and time 51.75 s, phase of the barotropic velocity $\phi \approx \pi/2$. (*b*) Modal structure of the baroclinic field.

M	Subcritical	Critical	Supercritical
DNS	0.56 ± 0.01	0.67 ± 0.01	0.92 ± 0.02
Pétrélis *et al.* (2006)	0.56	0.59^a	0.95 ± 0.02^b

TABLE 2. Conversion factor (M) at $Re_s = 30$. [a] M increases from 0.59 to 0.77 abruptly as ϵ changes from 1 to 1.05. [b] The value is not quoted and the error band is associated with the digitization of figure 5(*a*) in Pétrélis *et al.* (2006).

in supercritical flow at $z \approx 0.75$ m and $z \approx 0.02$ m correspond to the primary generated beam with group velocity directed upwards and a secondary beam formed by bottom reflection of the downward generated beam, respectively.

Modal analysis is performed using the time series of the baroclinic component of the vertical velocity profiles at the location $x = R = 3$ m (see appendix B) and the corresponding modal structure is shown in figure 4(*b*). The supercritical flow has a relatively wide range of active modes. The sinusoidal structure superimposed on the decaying profile of the modal distribution in supercritical flow is due to the presence of two beams which have vertical components of the group velocity in opposite directions at the generation region. The number of modes required to contain a given percentage of the total energy increases from the subcritical to supercritical flow: in subcritical flow, the first 9 modes are sufficient to represent 90 % of the total energy whereas critical and supercritical flows require the first 30 and 50 modes, respectively.

3.4. *Radiative conversion*

The radiative conversion factor, M in (B 3), is the value of the radiated wave energy flux integrated over the boundary of a domain enclosing the topography and normalized with $\pi \rho_0 U^2 h^2 \sqrt{(N^2 - \Omega^2)}/4$. The quantity M is computed at $Re_s = 30$ for three different values of ϵ and presented in table 2 along with the analytical estimate given by Pétrélis *et al.* (2006) using inviscid linear theory. In both theory and simulations, the conversion to radiated wave flux increases from subcritical to
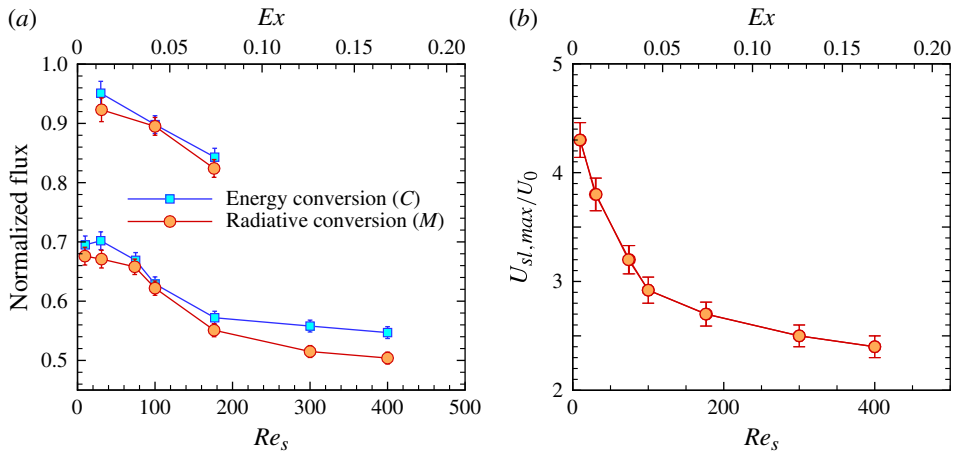
FIGURE 5. (Colour online) The effect of increasing barotropic forcing on: (*a*) the normalized radiated baroclinic flux and the energy conversion in critical (bottom two curves) and supercritical (top two curves) cases; and (*b*) the intensification of near-bottom velocity in critical cases.

supercritical flow. The simulations agree well with the theory in subcritical and supercritical cases. However, the linear theory underestimates the radiated flux when $\epsilon \sim O(1)$ in agreement with Khatiwala (2003). Note that, as shown in figure 1(*b*), the critical length on the slope of the smoothed triangular ridge is shorter than the triangular ridge used in the linear analysis by Pétrélis *et al.* (2006). This is due to the smoothing performed at top and bottom of the ridge to avoid numerical instabilities during the simulation. The value of M in critical flow DNS would be even higher than 0.67 if the level of smoothing was decreased.

4. Effect of forcing on the internal wave field in the critical slope case

The decrease of radiative conversion factor, M, i.e. the normalized wave flux, with increasing forcing is a major result of this paper. As shown in figure 5(*a*), with increasing forcing, thereby Re_s and Ex, the quantity M (the line with circles) in the critical slope cases 1–7 decreases in the laminar regime, has a sharper decrease when the flow transitions to turbulence at $Re_s \simeq 100$, and eventually exhibits a gradual drop at the higher values of forcing. The value of M in case 7 with $Re_s = 400$, $Ex = 0.168$ is reduced by 25 % of the peak to a value that is even lower than that in the corresponding subcritical case. The energy conversion factor, C, decreases and will be discussed in § 4.1 on the baroclinic energy budget. In the present series of simulations, when forcing is increased, extensive patches of three-dimensional turbulence fluctuations are seen at $Re_s \simeq 100$ and above. In figure 5(*b*), intensification of the along slope velocity is shown as a function of Re_s and Ex. The intensification drops owing to increased drag and mixing of momentum. It is also found (not shown) that the intensification during downslope flow is greater than that during upslope flow. It is of interest to compare the normalized wave flux in the case with $Re_s = 177$ in the present flow over a ridge with that for a single-slope topography with similar length and with $Re_s = 177$ given by Gayen & Sarkar (2011*b*). The present case with two slopes and, consequently, a beam on each side of the topography has approximately twice the normalized flux, $M = 0.28$, of the single-sloped topography.
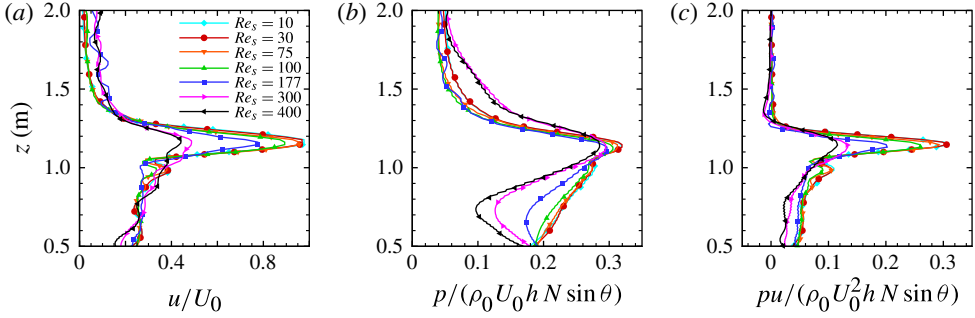
FIGURE 6. (Colour online) Vertical profiles of the normalized values of: (*a*) baroclinic velocity amplitude; (*b*) baroclinic pressure amplitude; and (*c*) the product of pressure and velocity amplitudes. Profiles shown at $x = -3$ m, a location away from the topography.

To compute M, the vertically integrated values of cycle-averaged outgoing energy flux, $\widehat{p_{bc}u_{bc}}$, were computed at $x = \pm 3$ m, summed and then normalized. To further understand the decrease of M, the vertical profiles at $x = 3$ m of the amplitude of p_{bc} computed as the root mean square of $p_{bc}(z, t)$, and the amplitude of u_{bc}, computed similarly, are plotted in figure 6(*a,b*). The peak velocity amplitude occurs in the internal wave beam and drops with increasing Re_s when Re_s exceeds 75. This decrease in velocity is the primary reason for the drop of peak wave energy flux seen in figure 6(*c*).

Figure 7(*a*) shows the effect of forcing, denoted by Re_s, on frequency spectra at locations A and B, shown earlier in figure 2. The contribution of the higher harmonics relative to the fundamental increases with increasing forcing. In the case with $Re_s = 10$ without turbulence, the continuous spectrum at frequencies beyond N_∞ is identical between A and B. The higher Re_s cases show significantly higher energy beyond the buoyancy frequency at point A in the boundary layer and, although at a somewhat lower level, also at point B in the beam. In these higher Re_s cases, the energy at $\omega > N_\infty$ resides both at discrete peaks corresponding to evanescent internal waves and a broadband continuous component that corresponds to turbulence. Most of the energy is carried by the fundamental frequency. In general, away from the generation region, more than 90 % of the energy is carried by the fundamental frequency. Hence, the modal analysis is performed for the fundamental frequency even for the turbulent flow simulations. The modal amplitudes are shown in figure 7(*b*). When forcing (Re_s, Ex) increases, the peak modal amplitude decreases as can be anticipated from the systematic decrease of the peak of velocity profile with increasing forcing that was seen in figure 6(*a*). Interestingly, the amplitude of the higher modes decrease substantially in the simulations with $Re_s \geqslant 100$. We will show later that the conversion to turbulence (measured by turbulent production) also increases substantially when $Re_s \geqslant 100$.

4.1. *Baroclinic energy budget*

In the case of inviscid theory, the internal wave flux is equal to the conversion from the barotropic to the baroclinic wave field. DNS/LES allows the separation of effects of forcing on conversion from those on wave flux. The velocity is split into a mean field (computed by spanwise averaging) and a three-dimensional fluctuation field, e.g. $u(x, y, z, t) = \langle u \rangle (x, z, t) + u'(x, y, z, t)$. The mean field is then partitioned
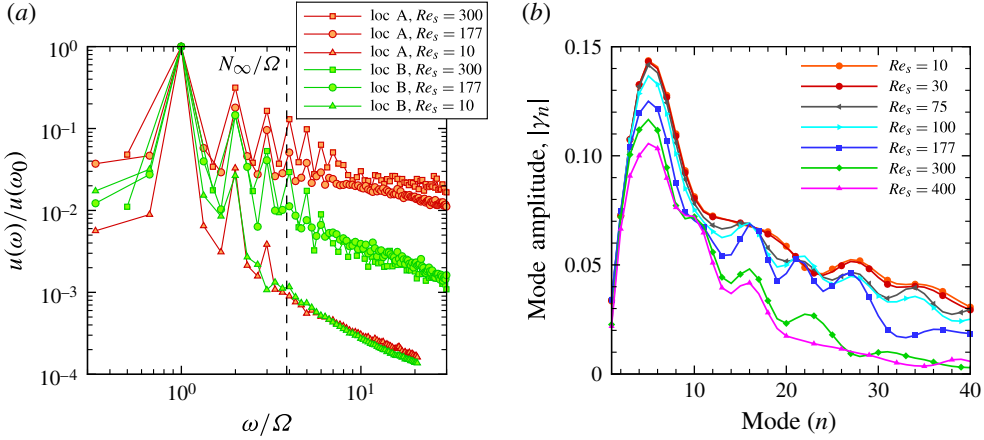
FIGURE 7. (Colour online) The effect of forcing in the critical slope case: (*a*) frequency spectra, with point A in the boundary layer (shown in red in the online version) and point B in the beam (shown in green in the online version); and (*b*) modal distribution at $x = 3$ m.

into a barotropic and a baroclinic component as follows and as further discussed in appendix A,

$$\langle u \rangle = U + u_{bc}, \quad \langle w \rangle = W + w_{bc}, \quad \langle p^* \rangle = P^* + p_{bc},$$

where p^* is the deviation from the hydrostatic pressure. Here U, W, P^* are the barotropic components and u_{bc}, w_{bc}, p_{bc} are baroclinic components defined such that U, P^* are the depth average of $\langle u \rangle, \langle p^* \rangle$, respectively, and $W(z) = -\partial/\partial x([z - h(x)]U)$. The buoyancy is defined as $b \equiv -g\langle \rho^* \rangle/\rho_0$ where ρ^* is the deviation from the background density.

The equation for the baroclinic energy (see Carter *et al.* 2008; Kang & Fringer 2012) with advective and diffusive fluxes of the wave energy neglected is

$$\frac{\partial}{\partial t}(\overline{KE} + \overline{PE}) + \nabla \cdot \overline{\boldsymbol{F}} = \overline{C} - \overline{\varepsilon}_{bc} - \bar{P}, \quad (4.1)$$

where

$$KE = \frac{1}{2}(u_{bc}^2 + v_{bc}^2 + w_{bc}^2), \quad PE = \frac{1}{2}N^{-2}b^2, \quad \boldsymbol{F} = p_{bc}\boldsymbol{u}_{bc}, \quad C = \frac{\partial p^*}{\partial z}W, \quad (4.2)$$

$$\varepsilon_{bc} = \nu \frac{\partial (u_{bc})_i}{\partial x_j} \frac{\partial (u_{bc})_i}{\partial x_j}, \quad P \equiv -\langle u_i'u_j' \rangle_y \langle S_{ij} \rangle_y - \langle \tau_{ij} \rangle_y \langle S_{ij} \rangle_y. \quad (4.3)$$

The overbar represents depth integration, $\bar{C}$ represents conversion from the barotropic to baroclinic wave field, $\overline{\varepsilon}_{bc}$ represents viscous dissipation of the baroclinic energy and $\overline{\boldsymbol{F}}$ represents the linear wave energy flux. The term, $-\bar{P}$, is not present in Kang & Fringer (2012) but is required here to account for turbulence. In the turbulent kinetic energy (TKE) equation, P appears with a positive sign on the right-hand side and is commonly referred to as turbulent production since P is generally (but not always) a source for TKE. In the absence of a density field and at $Re_s = 177$, the flow is laminar; therefore, all of the turbulence in the present case with density stratification is associated with the baroclinic field. Therefore, in the present context, P can be interpreted as local conversion from the internal tide to turbulence. Here τ_{ij} is the SGS

Case	Re_s	Ex	Tendency	Conversion to waves (C)	Wave flux (F_{bc} or M)	Baroclinic dissipation (ε_{bc})	Turbulent production (P)	Residual
1	10	0.004	0.009	0.695	0.676	0.030	—	−0.020
2	30	0.013	0.011	0.702	0.671	0.027	—	−0.007
3	75	0.031	−0.005	0.669	0.658	0.020	—	−0.004
4	100	0.042	−0.008	0.629	0.622	0.018	0.022	−0.025
5	177	0.074	−0.008	0.572	0.551	0.013	0.025	−0.009
6	300	0.126	−0.001	0.558	0.515	0.011	0.061	−0.028
7	400	0.168	−0.009	0.547	0.504	0.010	0.051	−0.009
2sup	30	0.013	−0.008	0.951	0.923	0.017	—	0.019
4sup	100	0.042	−0.005	0.898	0.895	0.012	0.011	−0.015
5sup	177	0.074	−0.008	0.843	0.824	0.007	0.028	−0.008

TABLE 3. Baroclinic energy budget, integrated over an area of the computational domain from $x = -3$ to $x = +3$ m and averaged over three tidal cycles, in the critical slope cases. All terms are normalized with $(\pi/4)\rho_0 U^2 h^2 \sqrt{(N^2 - \Omega^2)}$.

stress tensor discussed in § 2.2. The bottom drag term that appears in Kang & Fringer (2012) is not present in (4.1) since viscous effects at the bottom are resolved in the present study without recourse to any explicit drag parameterization in the momentum conservation equation.

At steady state, the conversion from barotropic to baroclinic tide, $\bar{C}$, is balanced by the radiative conversion, $\nabla \cdot \bar{F}$, in the linear inviscid approximation. In general, there are two additional terms, the viscous dissipation, $\bar{\varepsilon}_{bc}$, of the mean field and the conversion to turbulence, $\bar{P}$. The radiative conversion was shown earlier to decrease with increasing forcing. We now assess the behaviour of the other terms in the baroclinic energy balance. Each term in (4.1) is integrated over $-3 < x < 3$ m in the horizontal direction, averaged over three tidal cycles, normalized by $(\pi/4)\rho_0 U^2 h^2 \sqrt{(N^2 - \Omega^2)}$, and shown in table 3. The residual, computed as the sum of all terms in (4.1) with the tendency and flux terms taken to the right-hand side, is generally small and ranges from 1 to 5 % of the conversion.

The primary inference from table 3 is that the initial drop of the wave flux from the laminar case, $Re_s = 30$, is primarily associated with a reduction in conversion. An additional contribution to the decrease in wave flux is the increasing value of conversion to turbulence, $\bar{P}$, which reaches approximately 10 % of the energy conversion, $\bar{C}$, at higher values of Re_s. The viscous dissipation, $\bar{\varepsilon}_{bc}$, of the mean baroclinic component decreases substantially in the turbulent flow cases, owing to reduced baroclinic shear.

5. Turbulence at the ridge in case 5 with critical slope

In this section, turbulence near the ridge in case 5 is characterized by computing the statistics at three different locations: the centre of the left slope of the ridge ($x = -0.77$ m), a location where the left slope experiences a change in its slope ($x = -0.4$ m) and near the centre of the ridge ($x = -0.1$ m), represented by the dashed vertical lines in red, white and black in figure 8(a), respectively. Since the ridge is symmetric about $x = 0$, the dynamics on the right slope of the ridge are similar to those on the left but with a phase difference of approximately 180° and hence are not discussed.
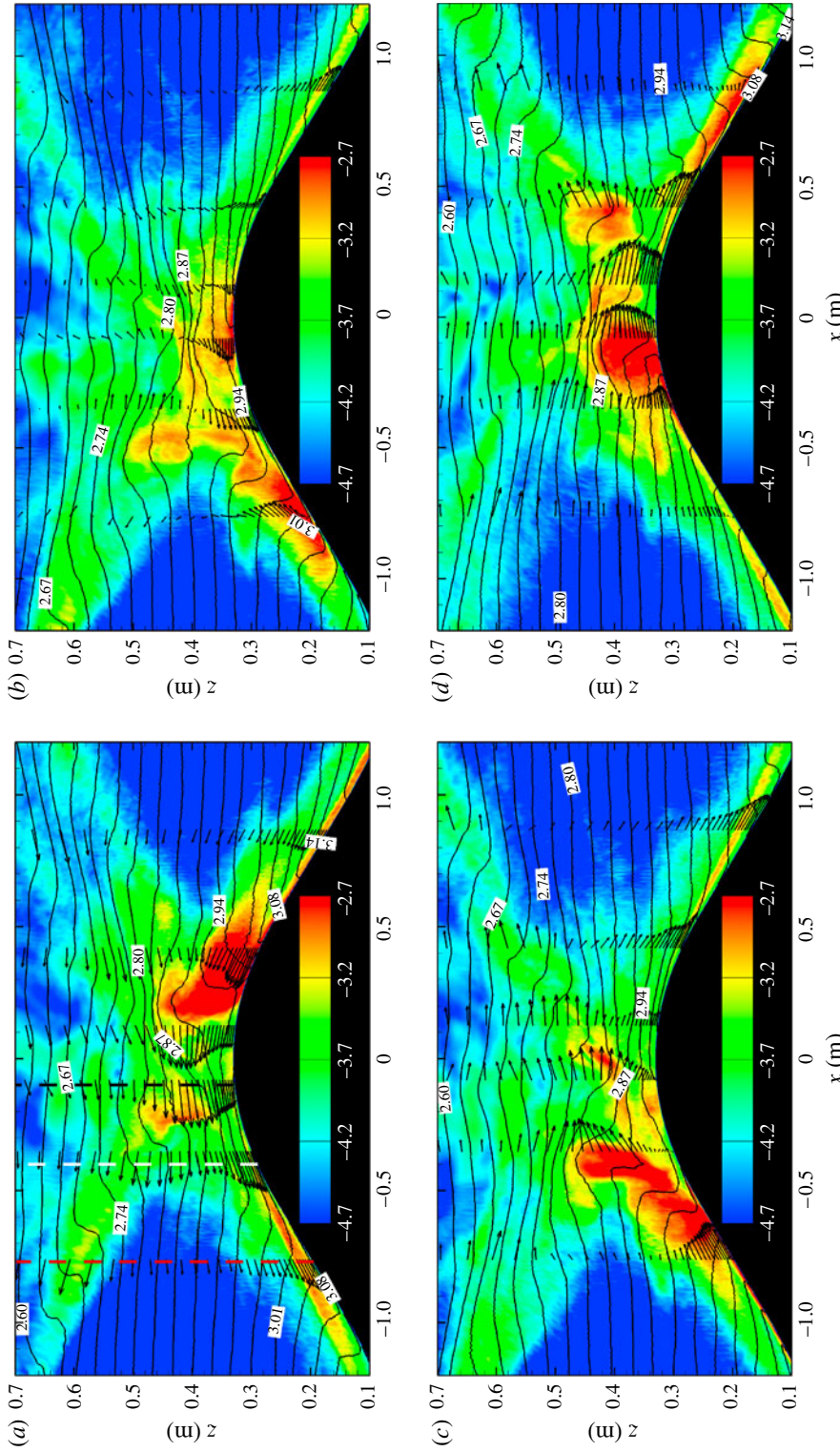
FIGURE 8. Plots of $\log_{10}$(TKE) and isopycnals near the topography in case 5 are shown in (*a*–*d*) at times 42.5, 44, 44.8 and 46.3 s. These times correspond to phase -90 (peak downslope velocity), 0, 90 and 180 of the streamwise velocity at $x = -0.77$ m in the beam centre, respectively, not with respect to the barotropic velocity. The dashed vertical lines in red, white and black in (*a*) indicates $x = -0.77$ m (midslope), -0.4 and -0.1 m, respectively. The forcing time period is $T = 2\pi$ s and the ridge height is $h = 0.328$ m.

The governing equation for TKE, $K = 1/2 \langle u_i' u_i' \rangle_y$, is given below:

$$\frac{\partial K}{\partial t} + \langle u \rangle_y \frac{\partial K}{\partial x} + \langle w \rangle_y \frac{\partial K}{\partial z} = P - \varepsilon + B - \frac{\partial T_x}{\partial x} - \frac{\partial T_z}{\partial z}. \qquad (5.1)$$

Here, T is the transport of TKE including pressure transport, turbulent transport, viscous transport and subgrid scale (SGS) transport,

$$T_x \equiv \frac{1}{\rho_0} \langle p' u' \rangle_y + \frac{1}{2} \langle u_i' u_i' u' \rangle_y - \nu \frac{\partial K}{\partial x} + \langle \tau_{i1}' u_i' \rangle_y \qquad (5.2)$$

$$T_z \equiv \frac{1}{\rho_0} \langle p' w' \rangle_y + \frac{1}{2} \langle u_i' u_i' w' \rangle_y - \nu \frac{\partial K}{\partial z} + \langle \tau_{i3}' u_i' \rangle_y \qquad (5.3)$$

and P is the production term, defined in (4.1). The turbulent dissipation rate, ε, is defined as the sum of the resolved and SGS components:

$$\varepsilon \equiv \nu \left\langle \frac{\partial u_i'}{\partial x_j} \frac{\partial u_i'}{\partial x_j} \right\rangle_y - \langle \tau_{ij} S_{ij} \rangle_y. \qquad (5.4)$$

Finally, B is the buoyancy flux defined as

$$B \equiv -\frac{g}{\rho_0} \langle \rho' w' \rangle_y. \qquad (5.5)$$

Figure 8(*a*–*d*) display snapshots of TKE, isopycnals and velocity profiles near the topography at different times over a tidal cycle. Turbulence across the ridge is inhomogeneous in both the streamwise and vertical directions. TKE patches are spread across the topography with varying magnitude and thickness. Close to the centre of the ridge, TKE shows structures of large vertical extent. The phasing of turbulence relative to the near-bottom velocity was discussed by Gayen & Sarkar (2011*a*) who assumed an internal wave beam profile with streamwise homogeneity that allowed LES of a thick beam with width of approximately 60 m and *M*2 forcing of 12.4 h. There is an important similarity (turbulence generation by convective instability during flow reversal from down to up) and an important difference (large shear production) in the present problem. The difference is because, by construction, the streamwise periodic boundary conditions employed by Gayen & Sarkar (2011*a*) to study the evolution of the stratified bottom jet that forms during critical slope generation did not allow the inhomogeneous wave propagation found here. Furthermore, there are substantial differences near the top of the ridge because of the crossing of the two beams at opposite sides, a phenomenon not present in either the turbulent beam simulation of Gayen & Sarkar (2011*a*) or the simulation of generation at a slope by Gayen & Sarkar (2011*b*).

The times shown in figure 8 are chosen on the basis of near-bottom velocity at $x = -0.77$ m, a midlocation on the left slope of the ridge: part (*a*) corresponds to peak downward velocity (taken to be phase -90), part (*b*) to zero velocity (phase 0), part (*c*) to peak upward velocity (phase 90), and part (*d*) to zero velocity (phase 180). Figure 8(*a*) shows downward flow over the entire left slope and a thin turbulent layer of thickness approximately equal to the beam width. Figure 8(*b*) shows a thicker turbulence patch on the left slope. At this time and at the midslope, $x = -0.77$ m, the near-bottom velocity is almost zero (taken to be phase of zero) and the near-bottom isopycnals show steepening to almost vertical. A convective instability associated with wave breaking is seen. The turbulent patch and the density front propagate upward as a bore. The vertical extent of the turbulence patch at phase 90 in figure 8(*c*) is
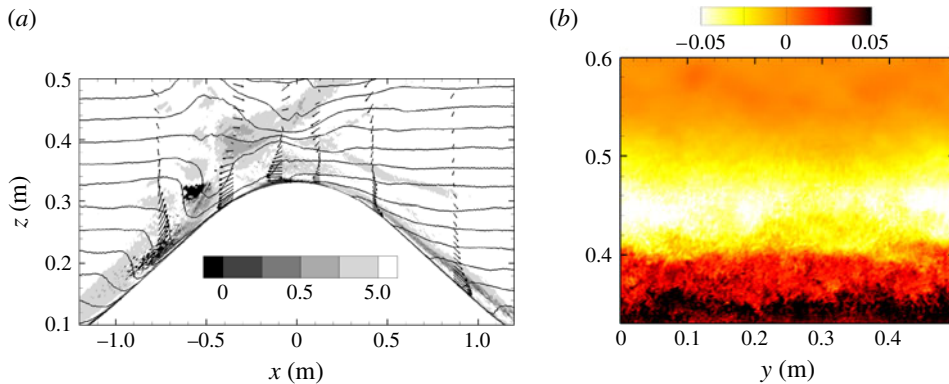
FIGURE 9. (Colour online) (*a*) Plot of Ri_g and isopycnals near the topography in case 5 is shown at time 44 s corresponding to phase 0 of the streamwise velocity at $x = -0.77$ m in the beam centre. (*b*) Density perturbations in the spanwise vertical plane at the centre of the ridge ($x = 0$ m) shown at time 25.2 s corresponding to phase 0 of the streamwise velocity for case 5. The forcing time period is $T = 2\pi$ s and the ridge height is $h = 0.328$ m.

largest at $x \simeq -0.4$ m and spans a region of reduced stratification as can be seen by the increased distance between isopycnals. At phase 180, shown in figure 8(*d*), there is turbulence at the top of the ridge.

The location of turbulence relative to the near-bottom velocity is of interest. The initiation of turbulence on the critical slope, shown in figure 8(*b*), corresponds to flow reversal from down to up, similar to Gayen & Sarkar (2011*a*), when the local near-bottom velocity passes through zero and there is a convective overturn. The convective overturns that are seen at this phase in the present critical slope case followed by bore-like features are similar to those noted by Legg & Klymak (2008) in their study of a strongly supercritical ($\epsilon = 4$) ridge. However, an important difference is that, unlike Legg & Klymak (2008) who find overturns in the lee (rearward with respect to the flow on the ridge) of the topography, we find overturns both on the windward side (figure 8*a*,*c*) and on the leeward side (figure 8*b*,*d*).

The gradient Richardson number, $Ri_g(x, z) = N^2(x, z)/S^2(x, z)$ where N is the mean buoyancy frequency and S is the mean shear, is an indicator of unstable regions. Figure 9(*a*) is an example corresponding to the time instant corresponding to figure 8(*b*). Convectively unstable regions ($Ri_g < 0$) and regions susceptible to shear instability ($0 < Ri_g < 0.25$) can be seen clearly. Consequently, the evolution of terms in the TKE balance to be discussed below show that both positive buoyancy flux and positive shear production lead to TKE generation. In figure 9(*b*), the density perturbations in the spanwise plane at the ridge centre ($x = 0$) are shown at time 25.2 s corresponding to phase 0. It shows three-dimensionality of the flow in case 5.

To understand the phase dependence, the evolution of vertical profiles of turbulence statistics at the midslope $x = -0.77$ m is shown in figure 10(*b*–*e*) over two tidal cycles after the simulation has reached a quasi-steady state. Note that the simulations are performed for nine tidal cycles and the quasi-steady state is observed after five cycles. In figure 10(*a*) the evolution of the mean velocity and the density profiles at different z locations ($z = 0.2$ m to $z = 0.28$ m) are shown. Upper to lower z locations are represented by lighter to darker lines, respectively. The time series data leads to the following results: (i) there is significant asymmetry between upslope and downslope
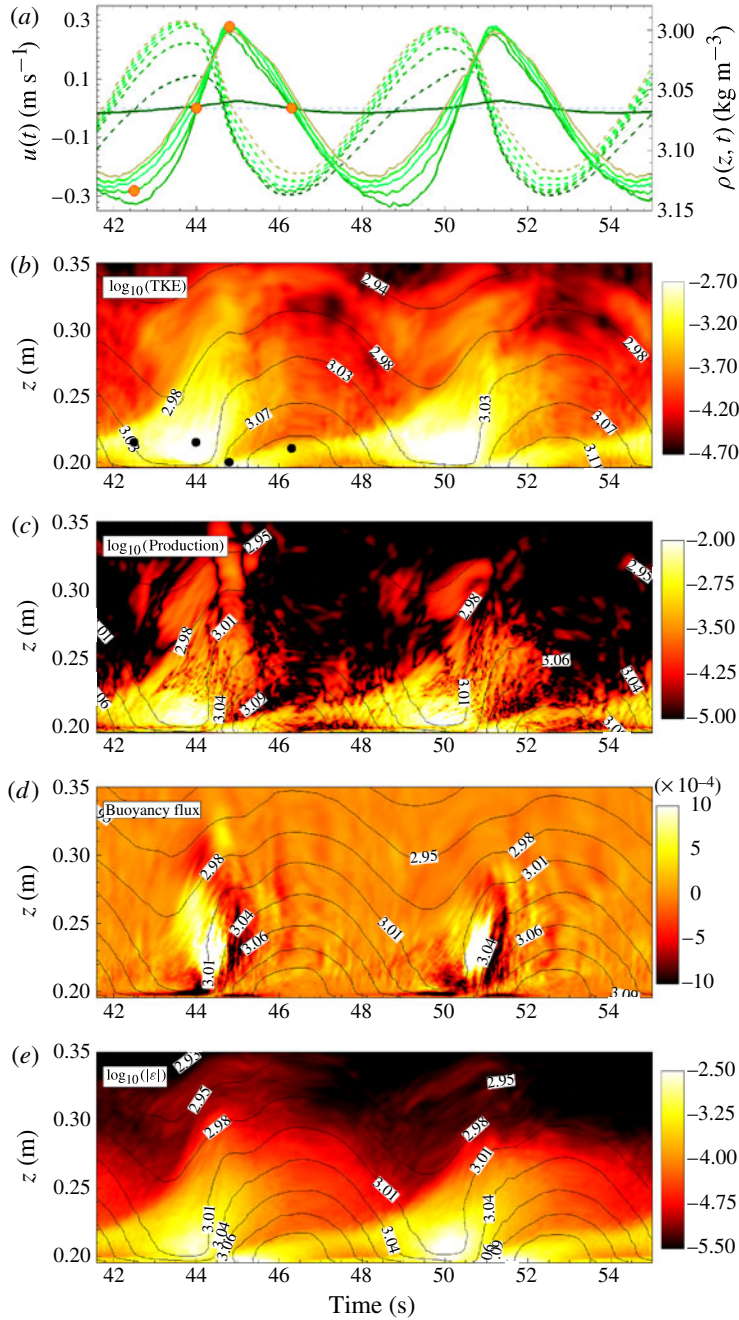
FIGURE 10. (Colour online) Flow and turbulence in case 5 at $x = -0.77$ m, the centre of the left slope of ridge: evolution of (*a*) streamwise velocity (solid lines) and density (dashed lines) at various locations, $z = 0.2$ m (the darkest) to $z = 0.28$ m (the lightest); (*b*) TKE, m^2 s^{-2}; (*c*) production, m^2 s^{-3}; (*d*) buoyancy flux, m^2 s^{-3}; and (*e*) dissipation, m^2 s^{-3}. The solid lines in black in (*b*–*e*) represent isopycnals. Four filled circles shown at times 42.5, 44, 44.8 and 46.3 s are used to illustrate the phase dependence of the statistics. The forcing time period is $T = 2\pi$ s and the ridge height is $h = 0.328$ m.

flow, e.g. the upslope flow shows a rapid acceleration (corresponding to an upslope bore, also seen previously by Gayen & Sarkar (2011*b*)) and it occupies a shorter duration of the cycle; (ii) there is significant asymmetry between acceleration and deceleration stages; (iii) the density lags behind the velocity by a substantial amount, as much as 90° phase during some stages of the cycle; and (iv) the stratification is significantly reduced during some portions of the cycle. The evolution of statistics shown begins with a phase corresponding to the peak downslope velocity.

In figure 10(*b*), four distinct phases can be observed in the periodic evolution of TKE, each indicated by a black circle in that figure and by a corresponding grey circle (orange in the online version) in the streamwise velocity evolution of figure 10(*a*). The first black circle at $t = 42.5$ s corresponds to the phase of maximum downslope velocity during which TKE is prominent in a small region slightly above the bottom wall, around $z = 0.2$ m. At this phase, turbulence is shear driven as reflected by the presence of significant production in figure 10(*c*) and absence of positive buoyancy flux. The second circle at $t = 44$ s corresponds to down-to-upslope flow reversal during which a large TKE structure extending from the wall at $z = 0.2$ m to $z = 0.27$ m is observed. Notably, the buoyancy flux at this time, corresponding to the flow reversal, is positive. The reason is that continued downslope flow replaces the heavier fluid in the jet core region with lighter fluid from the top. The corresponding density profile has a positive gradient in the region above the peak velocity; an unstable configuration that results in turbulent overturns. Density inversions can also be seen in figure 10(*a*) where the heavier density lines shown in dark cross the lighter density ones. The third circle at $t = 44.8$ s corresponds to maximum upslope velocity during which TKE is prominent in a thin region with vertical extent of $z \approx 0.01$ m, attached to the bottom wall. The buoyancy flux is negative and the shear production is positive signifying that the TKE is largely due to shear and not convective instability. The fourth circle at $t = 46.3$ s corresponds to up-to-downslope flow reversal during which TKE is somewhat elevated. The turbulent dissipation shown in figure 10(*e*) is similar to the TKE and shows patches associated with wave breaking that originate away from the boundary as well as boundary patches associated with boundary layer shear.

We now describe the behaviour at $x = -0.4$ m, a location where there is a change in the slope angle from the critical value. Figure 11(*a*) shows the evolution of streamwise velocity and density at various locations, $z = 0.29$ m to $z = 0.39$ m. There are some differences with respect to the previously shown midslope location since $x = -0.4$ m is closer to the centre of the ridge and the outer portion of the profiles is influenced by the beam from the other side of the ridge leading to substantial distortion of the isopycnals. For instance, the first circle in figure 11(*b*) shows TKE at a larger distance away from the bottom relative to the corresponding phase at the midslope. The cause is a density overturn that appears at $z \approx 0.45$ m due to the interaction with the outer beam and, correspondingly, a positive value of buoyancy flux. The TKE corresponding to the second circle at $t = 44.8$ s is significant up to larger heights (twice as much compared with that at $x = -0.77$ m). At this time, the positive buoyancy flux is more detached from the boundary relative to similar phase at $x = -0.77$ m. The outer beam contributes to development of a wider density overturn and positive density deviation. The other two phases, one with peak bottom shear and the other with restratification, indicated by third and fourth circles in figure 11(*b*) are qualitatively similar to those in figure 10(*b*). The evolution of the dissipation is similar to the TKE and is not shown.

We now turn to the evolution of turbulence near the top of the ridge, $x = -0.1$ m where the behaviour is found to be qualitatively different from that at midslope as can be seen by comparing figure 12 with figure 10. The reason is that leftward
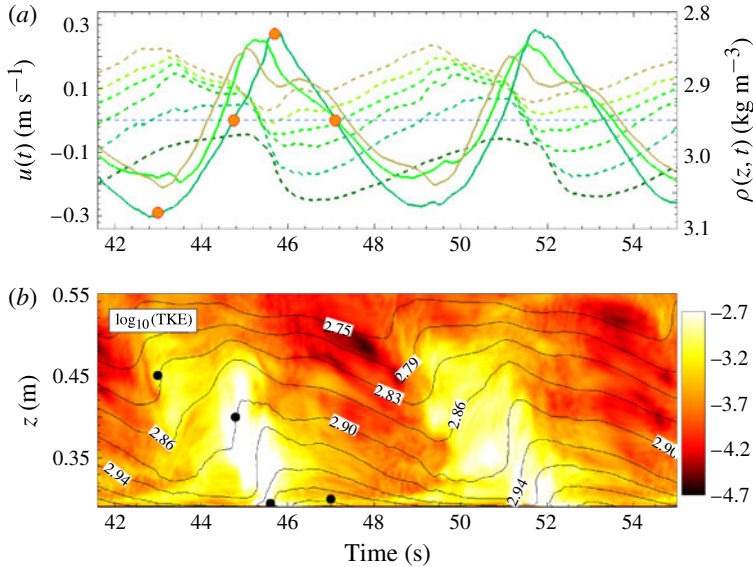
FIGURE 11. (Colour online) Flow and turbulence in case 5 at $x = -0.4$ m, end of the left slope of ridge: (*a*) evolution of streamwise velocity (solid lines) and density (dashed lines) at various locations, $z = 0.29$ m (the darkest) to $z = 0.39$ m (the lightest); and (*b*) TKE, m² s⁻². The solid lines in black represent isopycnals. Four filled circles shown at times 43, 44.8, 45.6 and 47 s are used to illustrate the phase dependence of the statistics. The forcing time period is $T = 2\pi$ s and the ridge height is $h = 0.328$ m.

and rightward beams originating from the two slopes cross, leading to a significant interaction at $x = -0.1$ m. At the top of the ridge, there are two events of TKE with large vertical extent in a cycle in contrast to one such event per cycle at the midslope. Each of the four TKE events in figure 12(*b*), that shows the evolution over two tidal cycles, originates away from the boundary in a region where the isopycnals (black lines in the figure) show a lower stratification than the background value. The region of lower stratification moves downward with increasing time in figure 12(*b*) and so does the TKE. The downward propagating phase is consistent with the upward propagating energy in the internal wave field.

The TKE at given spatial regions varies over a cycle. Figure 14 shows the cycle variation of terms in the area-integrated TKE budget at three different regions: A, B and C, shown in figure 13. Figure 14(*a*), corresponding to the midslope region A, shows that, during $41 < t < 44.5$ s that spans peak downslope flow to flow reversal, primarily shear production as well as buoyancy flux and advection lead to accumulation ($-\partial K/\partial t$ is negative in the figure) of TKE and some dissipation. During the rest of the cycle, TKE decreases in time primarily by advection out of the region and also because of dissipation and mixing indicated by negative buoyancy flux. The behaviour in the adjacent region B, where the slope angle decreases from critical, is shown in figure 14(*b*). Early in the cycle, TKE accumulates as a result of advection from the critical slope region. Later, during $43.5 < t < 45$ s, there is accumulation of TKE owing to shear production, buoyancy flux and advection. At $t = 45$ s, TKE starts to decrease despite positive production and buoyancy because of the advection term, which is a sink of TKE during $45 < t < 46.5$ s. During the same time period of $45 < t < 46.5$ s, advection acts as a source for TKE in the adjacent region at the top
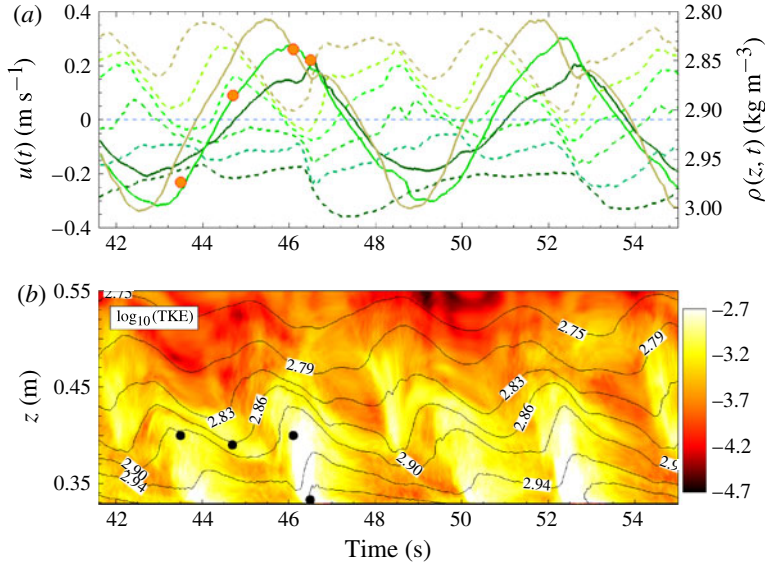
FIGURE 12. (Colour online) Flow and turbulence in case 5 at $x = -0.1$ m, close to the centre of the ridge: evolution of (*a*) streamwise velocity (solid lines) and density (dashed lines) at various locations, $z = 0.33$ m (the darkest) to $z = 0.43$ m (the lightest); and (*b*) TKE, m^2 s^{-2}. The solid lines in black represent isopycnals. Four filled circles shown at times 43.5, 44.7, 46.1 and 47.6 s are used to illustrate the phase dependence of the statistics. The forcing time period is $T = 2\pi$ s and the ridge height is $h = 0.328$ m.
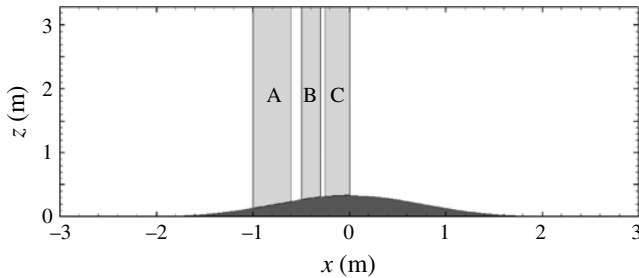

FIGURE 13. Shaded regions A, B and C correspond to a region on the critical slope ($-1 < x < -0.6$ m), a region where the slope changes from critical ($-0.5 < x < -0.3$ m) and a region at the top of the ridge ($-0.25 < x < 0$ m), respectively. These regions are used to analyse the evolution of the TKE budget terms shown in figures 14 and 16, and the cycle averaged TKE budget terms shown in table 4.

of the ridge as shown in figure 14(*c*). At the top of the ridge, region C, the primary balance is between advection and tendency terms. Temporal integration of the terms plotted in figure 14, shown in table 4, lead to the following result for cycle-averaged values. Turbulent production acts as the main source of TKE and it acts primarily at the critical slope and the top end of the critical slope. At the top of the ridge, advection from depth acts as the primary source of TKE. Cycle-averaged turbulent dissipation does not vary significantly among the three regions.
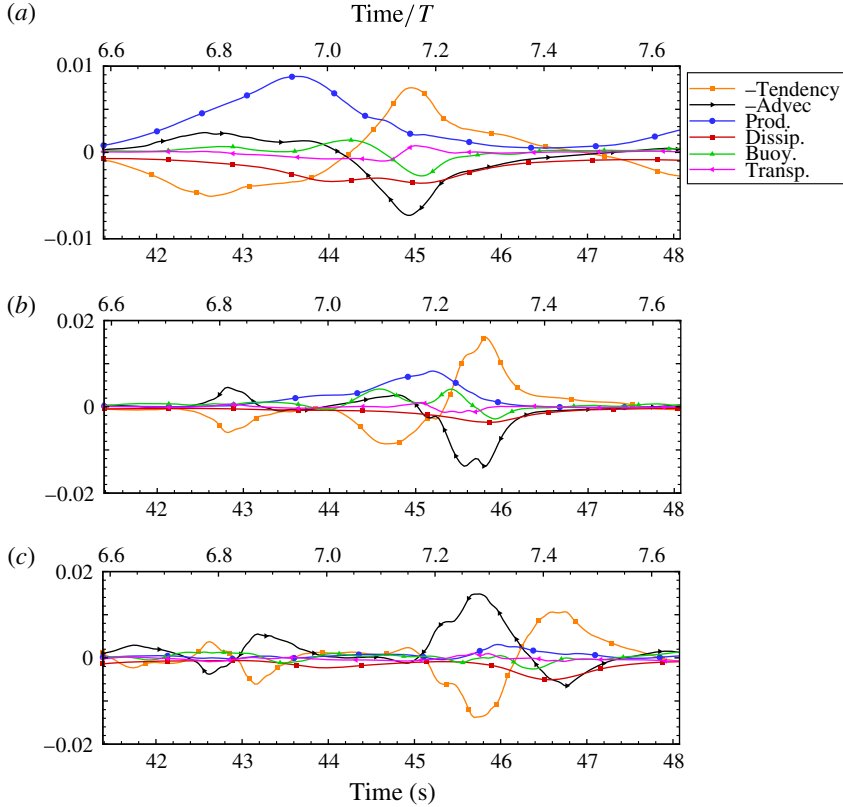
FIGURE 14. (Colour online) Evolution of TKE budget, integrated over three different areas shown in figure 13, (*a*) area A, (*b*) area B and (*c*) area C, as a function of tidal cycle. All terms are normalized by $(\pi/4)\rho_0 U^2 h^2 \sqrt{(N^2 - \Omega^2)}$. Note that $-\varepsilon$ (dissipation) and $-\partial K/\partial t$ (tendency) are plotted. The barotropic velocity is $U_0 \sin(2\pi t/T)$.

Case 5	Tendency	Advection	Production	Dissipation	Buoyancy	Transport
Area A	-2.19×10^{-4}	-7.45×10^{-4}	4.69×10^{-3}	-2.05×10^{-3}	-1.48×10^{-5}	2.77×10^{-5}
Area B	-1.38×10^{-5}	-9.51×10^{-4}	2.71×10^{-3}	-1.17×10^{-3}	5.78×10^{-4}	-2.25×10^{-4}
Area C	-5.38×10^{-5}	1.38×10^{-3}	1.44×10^{-3}	-1.61×10^{-3}	1.64×10^{-4}	-2.77×10^{-5}
Case 5sup	Tendency	Advection	Production	Dissipation	Buoyancy	Transport
Area A	4.78×10^{-5}	-7.46×10^{-6}	9.46×10^{-5}	-2.21×10^{-4}	-4.85×10^{-5}	2.22×10^{-5}
Area B	3.58×10^{-4}	3.66×10^{-4}	9.82×10^{-3}	-3.52×10^{-3}	-1.92×10^{-3}	-4.06×10^{-4}
Area C	4.63×10^{-5}	-5.98×10^{-4}	1.32×10^{-3}	-1.60×10^{-3}	-1.73×10^{-4}	1.09×10^{-4}

TABLE 4. Cycle averaged TKE budget, integrated over areas A, B and C (shown in figure 13), in the critical and supercritical slope cases. All terms are normalized with $(\pi/4)\rho_0 U^2 h^2 \sqrt{(N^2 - \Omega^2)}$.

6. Effect of forcing in the cases of subcritical and supercritical slopes

In simulations performed up to $Re_s = 177$, there was little turbulence in the subcritical case in contrast to the supercritical case. The normalized values of radiative and energy conversion exhibit little change.
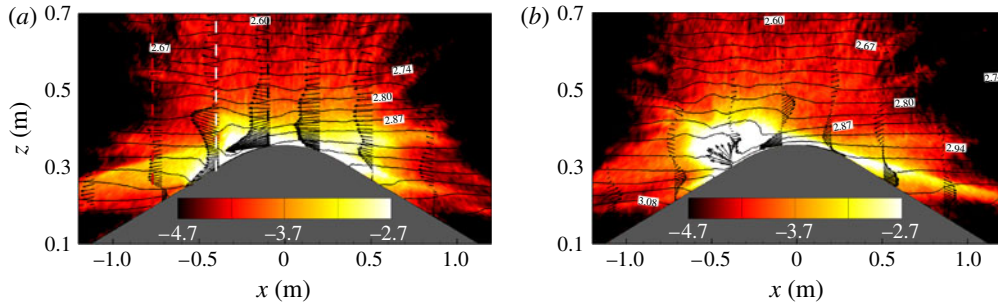
FIGURE 15. (Colour online) Supercritical case with $Re_s = 177$. $\log_{10}$(TKE) and isopycnals near the topography in case 5sup are shown in (a,b) at time 42.5 and 44 s, same as (a,b) of the corresponding figure 8 of the critical case. The dashed vertical lines (highlighted in red, white and black in the online version) in (a) indicate $x = -0.77$ m (midslope), -0.4 and -0.1 m, respectively.

To illustrate the characteristics of turbulence and the effect of forcing on the energy conversion in supercritical flow, three cases were investigated: $Re_s = 30$, 100 and 177, indicated by 2sup, 4sup and 5sup in table 1, respectively. At $Re_s = 30$, the flow is laminar and, for $Re_s = 100$ and above, the flow is turbulent.

Similar to the critical case, the normalized energy conversion in the supercritical cases decrease at higher forcing levels. The baroclinic energy budget for supercritical cases is included in table 3. The wave energy conversion and the wave radiative conversion decrease by 12.5 and 10.5 %, respectively, from $Re_s = 30$ to $Re_s = 177$ as the flow becomes turbulent. The baroclinic dissipation also decreases from $Re_s = 30$ to $Re_s = 177$, similar to the critical case. The turbulent production and dissipation increase with Re_s, similar to the critical case. Overall, the percentage decrease in conversion from $Re_s = 30$ to 177 in supercritical slope is smaller (12.5 %) compared with the critical slope (19 %). This is due to the smaller area over which turbulence is significant in the supercritical case relative to the critical case.

We will discuss turbulence in case 5sup and compare with the critical case 5 at the same value of $Re_s = 177$. Figure 15(a,b) display snapshots of TKE, isopycnals and velocity profiles near the topography corresponding to case 5sup at the same phases as figure 8(a,b), respectively, for case 5. TKE patches are clustered in a small region near the top of the ridge where the internal wave beam generation occurs. In contrast to case 5, the constant slope region in case 5sup is not critical and, therefore, does not have the significant level of TKE associated with breaking waves.

Figure 15(a) shows that TKE is present at both windward and leeward sides of the topography. Figure 15(b), corresponding to a later phase, shows elevated levels of TKE primarily on the leeward side in a region around $x = -0.4$ m where the slope is near-critical, and secondarily in the downward beam on the windward side. The large patch of turbulence around $x = -0.4$ m is associated with convective overturns and flow reversal from down to up discussed earlier in the critical case. However, the corresponding velocity profile at this time indicates stronger shear relative to the critical case 5 and, therefore, the turbulent production in this region is also significantly higher when compared to case 5 as will be shown.

TKE is generated primarily in a region (area B, shown in figure 13) above and adjacent to the constant slope region, where the slope angle transitions through the critical angle. Figure 16 shows evolution over a tidal cycle of the TKE budget
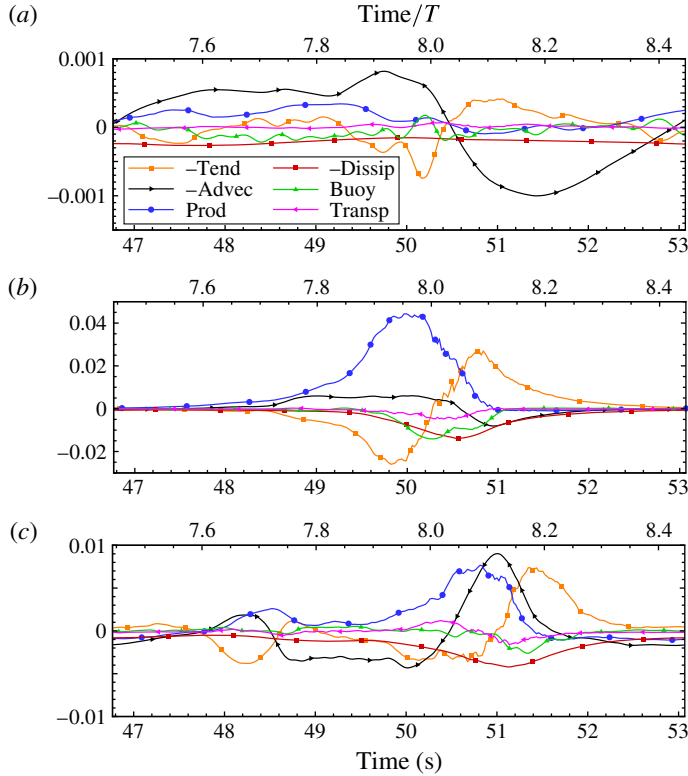
FIGURE 16. (Colour online) Supercritical case with $Re_s = 177$. Evolution of the TKE budget, integrated over three different areas shown in figure 13, (*a*) area A, (*b*) area B and (*c*) area C, as a function of the tidal cycle. All terms are normalized by $(\pi/4)\rho_0 U^2 h^2 \sqrt{(N^2 - \Omega^2)}$. Note that $-\varepsilon$ (dissipation) and $-\partial K/\partial t$ (tendency) are plotted. The barotropic velocity is $U_0 \sin(2\pi t/T)$.

integrated over three different areas, similar to case 5 shown in figure 14. Figure 16(*a*) shows that, in contrast to case 5, the budget terms at area A in the midslope region are an order of magnitude lower than the corresponding values in area B (figure 16*b*) and C (figure 16*c*). This behaviour is consistent with the finding that TKE levels are not significant at the constant slope region in case 5sup. In figure 16(*b*), area B exhibits strong shear production that is substantially larger than that at midslope or at the top of the ridge. The advection term indicates transport of the generated TKE from area B to area C between time 50.5 and 51.5 s. The shear production of TKE in area C near the top of the ridge, shown in figure 16(*c*), although smaller than that in area B, shown in figure 16(*b*), is also significant.

The cycle-averaged values of terms in the TKE budget are given in table 4. The largest production and dissipation of turbulence is over the critical slope region (area A of case 5 and area B of case 5sup) of the model ridge.

For completeness, the influence of forcing on the modal distribution in the supercritical and subcritical regime has been examined and the results are plotted in figure 17. The supercritical cases, similar to the critical cases, show that high modes are progressively eliminated when the forcing increases. On the other hand, subcritical
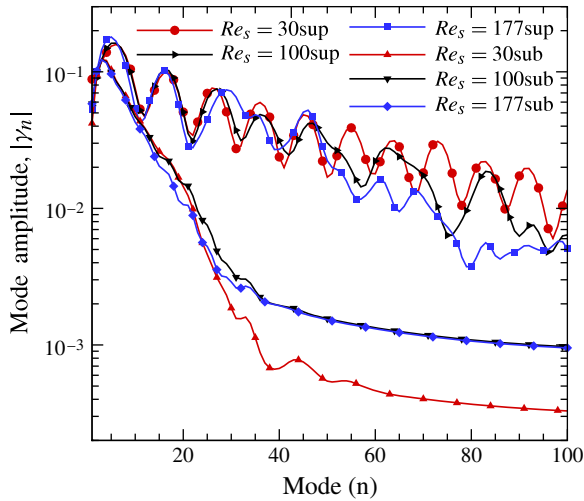
FIGURE 17. (Colour online) The effect of increasing barotropic forcing on modal distribution at $x = 3$ m in supercritical and subcritical cases.

cases where there is little turbulence, show an enhancement of energy content at the high modes with increased forcing.

7. Conclusions

Three-dimensional DNS and LES approaches have been used to examine the local flow as well as the radiated internal tide at a model ridge taken to have triangular topography. Nonlinear effects on the tidal energy conversion are examined by increasing the tidal forcing so that the excursion number increases, while remaining significantly smaller than unity, and the Reynolds number, Re_s, based on the Stokes boundary layer thickness also increases. Implications of the present work for linear predictions of internal wave flux from sloping topography in the regime of excursion number less than $O(1)$ are as follows. Linear theory works well in subcritical cases where there is little turbulence for all values of tidal forcing examined here and for supercritical cases with low forcing where there is also little turbulence. In critical or supercritical cases with higher forcing, the energy conversion to the internal waves decreases with increasing forcing, as much as 25 % in the present simulations compared with the laminar value.

Nonlinear effects on the tidal energy conversion are examined in the critical slope ridge by increasing the tidal forcing so that the excursion number increases from 0.004 to 0.168 and the Reynolds number, Re_s, increases from 10 to 400. The simulated cases with higher forcing exhibit wave breaking leading to a near-bottom layer of turbulence and upslope propagation of turbulent bores along with radiated internal wave beams. The internal wave energy flux is found to decrease substantially with the onset of turbulence. The radiative conversion (normalized wave flux) decreases to a value of $M \simeq 0.50$, smaller than the corresponding subcritical case, corresponding to a substantial reduction from the laminar value. Evaluation of the baroclinic energy balance shows that the decrease in M is associated with a decrease in normalized energy conversion, C, from the barotropic to baroclinic flow and additionally because of conversion to turbulence, i.e. the turbulent production, P. Modal analysis of the

radiated wave field shows that, with increasing forcing, not only does the peak modal amplitude decrease but also the high modes are progressively eliminated. The contribution of higher temporal harmonics relative to the fundamental increases with increasing forcing. Turbulence varies over a cycle with a systematic dependence on tidal phase and is found at both leeward and windward sides of the ridge. Both convective and shear instability mechanisms are found to initiate transition to turbulence within a cycle. There is a substantial variation in turbulence properties when comparing three locations: at the middle of the critical slope, at the upper ridge where the slope angle changes from critical to smaller values, and at the top of the ridge where internal wave beams from opposite sides interact.

Supercritical ridges also exhibit decreases in energy conversion and radiated wave flux with increasing forcing. In contrast to the critical slope case, turbulence is insignificant at the constant supercritical slope portion and is limited to the region between the critical portion and the top of the ridge. Owing to the reduced area of turbulence, the decrease in energy conversion is less in the supercritical case compared with the critical case. Turbulence is present at both leeward and windward sides of the ridge. Subcritical ridges do not exhibit turbulence in the range of parameters studied here and, correspondingly, the energy conversion factor shows little change.

Acknowledgements

Appendix A. Decomposition of pressure and velocity

Decomposition of the flow field into barotropic and baroclinic components is performed using the method described by Nash *et al.* (2004) except for pressure for which they impose hydrostatic balance. In the present work, since the pressure field is discretely available throughout the domain, we use the same procedure for pressure as that for the velocity field. The procedure for a generic spanwise-averaged variable $\phi(x, y, t) = \langle u \rangle, \langle p \rangle$ is summarized below.

The baroclinic component of $\phi(\mathbf{x}, t)$ is defined as

$$\phi_{bc}(\mathbf{x}, t) \equiv \phi(\mathbf{x}, t) - \widehat{\phi}(\mathbf{x}) - \phi_b(x, y, t) \tag{A 1}$$

where $\widehat{\phi}(\mathbf{x}) = \int_t^{T+t} \phi(\mathbf{x}, t) \, \mathrm{d}t/T$ is a cycle-averaged mean and $\phi_b(x, y, t)$ is calculated by enforcing baroclinicity:

$$\int_{h(x)}^{H} \phi_{bc}(\mathbf{x}, t) \, \mathrm{d}z = 0. \tag{A 2}$$

Here, $h(x)$ is height of the ridge topography with respect to the flat bottom.

Appendix B. Methods for modal analysis and conversion factor

The far-field vertical velocity that describes the linear baroclinic response to flow oscillating with frequency Ω over an isolated two-dimensional ridge in a linearly stratified finite-depth ocean is (see Pétrélis *et al.* 2006; Echeverri *et al.* 2009)

$$w_{bc}(X, Z, t) = \frac{U}{\mu} \mathrm{Re} \left\{ \sum_{n=1}^{\infty} \gamma_n \sin(nZ) \mathrm{e}^{\mathrm{i}(nX - \Omega t + \pi/2)} \right\}, \tag{B 1}$$

where

$$Z = \frac{\pi z}{H}, \quad X = \frac{\pi x}{\mu H}, \quad \mu = \frac{\sqrt{N_\infty^2 - \Omega^2}}{\Omega}. \tag{B 2}$$

Here, n is the mode number and γ_n is the mode amplitude.

The non-dimensional conversion factor, M, is given by (see Pétrélis *et al.* 2006),

$$M \equiv \frac{2 \int_0^h \boldsymbol{J}(x \geqslant l, z) \cdot \hat{\boldsymbol{x}} \, \mathrm{d}z}{\frac{\pi}{4} \rho h^2 U^2 \sqrt{N^2 - \Omega^2}} = \frac{2}{B^2} \sum_{n=1}^{\infty} \frac{\gamma_n \gamma_n^*}{n} \tag{B 3}$$

where $\boldsymbol{J}$ denotes the phase average of the baroclinic energy flux, $(p_{bc} u_{bc}, p_{bc} w_{bc})$, $\hat{\boldsymbol{x}}$ is the unit vector in the horizontal direction and $B = \pi h/H$.

The mode amplitude γ_n, is calculated as follows (see Echeverri *et al.* 2009). Define $\gamma_n = |\gamma_n| \mathrm{e}^{\mathrm{i}\phi_n}$ and project the baroclinic vertical velocity profile (the procedure used to extract baroclinic component from the simulated flow field is described in appendix A) at a location away from the topography, X, onto the sinusoidal vertical basis modes of the linear stratification:

$$\bowtie_n(t) \equiv \int_0^\pi w_{bc} \sin(nZ) \, \mathrm{d}Z = \left(\frac{\pi U}{2\mu} \right) |\gamma_n| \mathrm{Re}\{\mathrm{e}^{\mathrm{i}(\phi_n + nX - \Omega t + \pi/2)}\} \tag{B 4}$$

and the mode amplitude corresponding to the fundamental frequency is given by

$$|\gamma_n| = \frac{\frac{2}{T} \sqrt{\left(\int_0^T \bowtie_n \cos(\Omega t) \, \mathrm{d}t \right)^2 + \left(\int_0^T \bowtie_n \sin(\Omega t) \, \mathrm{d}t \right)^2}}{\left(\frac{\pi U}{2\mu} \right)} \tag{B 5}$$

where T consists of a complete number of wave periods associated with the fundamental frequency Ω.

REFERENCES

ARMENIO, V. & SARKAR, S. 2002 An investigation of stably stratified turbulent channel flow using large-eddy simulation. *J. Fluid Mech.* **459**, 1–42.

AUCAN, J., MERRIFIELD, M. A., LUTHER, D. S. & FLAMENT, P. 2006 Tidal mixing events on the deep flanks of Kaena Ridge, Hawaii. *J. Phys. Oceanogr.* **36**, 1202–1219.

BALMFORTH, N. J., IERLEY, G. R. & YOUNG, W. R. 2002 Tidal conversion by subcritical topography. *J. Phys. Oceanogr.* **32**, 2900–2914.

BELL, T. H. 1975a Lee waves in stratified fluid with simple harmonic time dependence. *J. Fluid Mech.* **67**, 705–722.

BELL, T. H. 1975b Topographically generated internal waves in the open ocean. *J. Geophys. Res.* **80**, 320–327.

CACCHIONE, D. A., PRATSON, L. F. & OGSTON, A. S. 2002 The shaping of continental slopes by internal tides. *Science* **296**, 724–727.

CARTER, G. S. & GREGG, M. C. 2002 Intense, variable mixing near the head of Monterey Submarine Canyon. *J. Phys. Oceanogr.* **32**, 3145–3165.

CARTER, G. S., MERRIFIELD, M. A., BECKER, J. M., KATSUMATA, K., GREGG, M. C., LUTHER, D. S., LEVINE, M. D., BOYD, T. J. & FIRING, Y. L. 2008 Energetics of m_2 barotropic-to-baroclinic tidal conversion at the Hawaiian islands. *J. Phys. Oceanogr.* **38**, 2205–2223.

ECHEVERRI, P., FLYNN, M. R., WINTERS, K. B. & PEACOCK, T. 2009 Low-mode internal tide generation by topography: an experimental and numerical investigation. *J. Fluid Mech.* **636**, 91–108.

FLETCHER, C. A. J. 1991 *Computational Techniques for Fluid Dynamics*, 2nd edn. Springer.

GAYEN, B. & SARKAR, S. 2010 Turbulence during the generation of internal tide on a critical slope. *Phys. Rev. Lett.* **104**, 218502.

GAYEN, B. & SARKAR, S. 2011*a* Boundary mixing by density overturns in an internal tidal beam. *Geophys. Res. Lett.* **38**, L14608.

GAYEN, B. & SARKAR, S. 2011*b* Direct and large eddy simulations of internal tide generation at a near critical slope. *J. Fluid Mech.* **681**, 48–79.

KANG, D. & FRINGER, O. 2012 Energetics of barotropic and baroclinic tides in the Monterey Bay area. *J. Phys. Oceanogr.* **42**, 272–290.

KHATIWALA, S. 2003 Generation of internal tides in an ocean of finite depth: analytical and numerical calculations. *Deep-Sea Res.* I **50**, 3–21.

KLYMAK, J. M., LEGG, S. & PINKEL, R. 2010 A simple parameterization of turbulent tidal mixing near supercritical topography. *J. Phys. Oceanogr.* **40**, 2059–2074.

KLYMAK, J. M., MOUM, J. N., NASH, J. D., KUNZE, E., GIRTON, J. B., CARTER, G. S., LEE, C, M., SANFORD, T. B. & GREGG, M. C. 2006 An estimate of tidal energy lost to turbulence at the Hawaiian ridge. *J. Phys. Oceanogr.* **36**, 1148–1164.

KUNZE, E. & TOOLE, J. M. 1997 Tidally driven vorticity, diurnal shear and turbulence atop Fieberling Seamount. *J. Phys. Oceanogr.* **27**, 2663–2693.

LEDWELL, J. R., MONTGOMERY, K. L., POLZIN, K. L., ST LAURENT, L. C., SCHMITT, R. W. & TOOLE, J. M. 2000 Evidence of enhanced mixing over rough topography in the abyssal ocean. *Nature* **403**, 179–182.

LEGG, S. & HUIJTS, K. M. H. 2006 Preliminary simulations of internal waves and mixing generated by finite amplitude tidal flow over isolated topography. *Deep-Sea Res.* II **53**, 140–156.

LEGG, S. & KLYMAK, J. 2008 Internal hydraulic jumps and overturning generated by tidal flows over a tall steep ridge. *J. Phys. Oceanogr.* **38**, 1949–1964.

LIM, K., IVEY, G. N. & JONES, N. L. 2010 Experiments on the generation of internal waves over continental shelf topography. *J. Fluid Mech.* **663**, 385–400.

LLEWELLYN SMITH, S. G. & YOUNG, W. R. 2002 Conversion of the barotropic tide. *J. Phys. Oceanogr.* **32**, 1554–1566.

LLEWELLYN SMITH, S. G. & YOUNG, W. R. 2003 Tidal conversion at a very steep ridge. *J. Fluid Mech.* **495**, 175–191.

LUECK, R. G. & MUDGE, T. D. 1997 Topographically induced mixing around a shallow seamount. *Science* **276**, 1831–1833.

MOUM, J. N., CALDWELL, D. R., NASH, J. D. & GUNDERSON, G. D. 2002 Observations of boundary mixing over the continental slope. *J. Phys. Oceanogr.* **32**, 2113–2130.

MUNK, W. & WUNSCH, C. 1998 Abyssal recipes II: energetics of tidal and wind mixing. *Deep-Sea Res.* I **45**, 1977–2010.

NASH, J. D., ALFORD, M. H., KUNZE, E., MARTINI, K. & KELLY, S. 2007 Hotspots of deep ocean mixing on the Oregon continental slope. *Geophys. Res. Lett.* **34**, L01605.

NASH, J. D., KUNZE, E., TOOLE, J. M. & SCHMITT, R. W. 2004 Internal tide reflection and turbulent mixing on the continental slope. *J. Phys. Oceanogr.* **34**, 1117–1134.

PÉTRÉLIS, F., LLEWELLYN SMITH, S. G. & YOUNG, W. R. 2006 Tidal conversion at submarine ridge. *J. Phys. Oceanogr.* **36**, 1053–1071.

POLZIN, K., OAKEY, N. S., TOOLE, J. M. & SCHMITT, R. W. 1996 Fine structure and microstructure characteristics across the north west Atlantic subtropical front. *J. Geophys. Res.* **101**, 14111–14121.

POLZIN, K. L., TOOLE, J. M., LEDWELL, J. R. & SCHMITT, R. W. 1997 Spatial variability of turbulent mixing in the abyssal ocean. *Science* **276**, 93–96.

RUDNICK, D. L., BOYD, T. J., BRAINARD, R. E., CARTER, G. S., EGBERT, G. D., GREGG, M. C., HOLLOWAY, P. E., KLYMAK, J. M., KUNZE, E., LEE, C. M., LEVINE, M. D., LUTHER, D. S., MARTIN, J. P., MERRIFIELD, M. A., MOUM, J. N., NASH, J. D., PINKEL, R., RAINVILLE, L. & SANFORD, T. B. 2003 From tides to mixing along the Hawaiian ridge. *Science* **301**, 355–357.

SLINN, D. N. & RILEY, J. J. 1998 Turbulent dynamics of a critically reflecting internal gravity wave. *Theoret. Comput. Fluid Dyn.* **11**, 281–303.

ST LAURENT, L. C. & GARRETT, C. 2002 The role of internal tides in mixing the deep ocean. *J. Phys. Oceanogr.* **32**, 2882–2899.

ST LAURENT, L. C., STRINGER, S., GARRETT, C. & PERRAULT-JONCAS, D. 2003 The generation of internal tides at abrupt topography. *Deep-Sea Res.* I **50**, 987–1003.

ST LAURENT, L. C., TOOLE, J. M. & SCHMITT, R. W. 2001 Buoyancy forcing by turbulence above rough topography in the abyssal Brazil Basin. *J. Phys. Oceanogr.* **31**, 3476–3495.

VREMAN, B., GEURTS, B. & KUERTEN, H. 1997 Large-eddy simulation of the turbulent mixing layer. *J. Fluid Mech.* **339**, 357–390.

WUNSCH, C. & FERRARI, R. 2004 Vertical mixing, energy, and the general circulation of the oceans. *Annu. Rev. Fluid Mech.* **36**, 281–314.

ZANG, Y., STREET, R. L. & KOSEFF, J. R. 1993 A dynamic mixed subgrid-scale model and its application to turbulent recirculating flows. *Phys. Fluids* A **5** (12), 3186–3196.

ZHANG, H. P., KING, B. & SWINNEY, H. L 2008 Resonant generation of internalwaves on a model continental slope. *Phys. Rev. Lett.* **100**, 244504.